This article has been accepted for inclusion in a future issue of this journal. Content is final as presented, with the exception of pagination.

TEMPEST-D Radiometer: Instrument Description and Prelaunch Calibration

Sharmila Padmanabhan, *Senior Member, IEEE*, Todd C. Gaier, Alan B. Tanner, Shannon T. Brown, *Senior Member, IEEE*, Boon H. Lim, *Senior Member, IEEE*, Steven C. Reising, *Senior Member, IEEE*, Robert Stachnik, Rudi Bendig, and Richard Cofield, *Life Member, IEEE*

***Abstract*— The Temporal Experiment for Storms and Tropical Systems Technology Demonstration (TEMPEST-D) instrument is a five-frequency millimeter-wave radiometer operating from 87 to 181 GHz. The cross-track scanning radiometer has been operating on a 6U CubeSat in low Earth orbit since September 5, 2018. The direct-detection architecture of the radiometer reduces its mass and power consumption by eliminating the need for a local oscillator and mixer, also reducing system complexity. The instrument includes a scanning reflector and ambient calibration target. The reflector rotates continuously to scan the antenna beams in the cross-track direction, first across the blackbody calibration target, then toward the Earth over the full range of incidence angles, and finally to cosmic microwave background radiation at 2.73 K. This enables precision end-to-end calibration of the millimeter-wave receivers during every 2-s scan period. The TEMPEST-D millimeter-wave radiometers are based on 35-nm indium phosphide (InP) high-electron-mobility transistor (HEMT) low-noise amplifiers. This article describes the instrument and its characterization prior to launch.**

***Index Terms*— Clouds, CubeSat, direct-detection receiver, microwave, millimeter-wave, monolithic microwave integrated circuit (MMIC), precipitation, radiometer.**

I. Introduction

THE TEMPEST mission was proposed to the NASA Earth Venture Instrument-2 announcement of opportunity in November 2013 as a closely spaced train of identical CubeSats to study the temporal evolution of precipitation using imaging millimeter-wave radiometers [1], [2]. At the time, CubeSat microwave radiometers had yet to be demonstrated in space, and NASA decided to fund a technology maturation program to demonstrate that the proposed millimeter-wave radiometer on a 6U CubeSat could provide science-quality data. The resulting mission, Temporal Experiment for Storms and Tropical Systems Technology Demonstration (TEMPEST-D), is necessary to establish the heritage for TEMPEST in a range of domains from science, instrument, and spacecraft to mission design and operations. The goal of TEMPEST-D is to reduce the risk, cost, and development time for future radiometric measurements of Earth science processes using CubeSat constellations. In addition, TEMPEST-D raises the technology readiness level (TRL) of the TEMPEST millimeter-wave radiometer instrument from TRL 5 to TRL 9. This mission also provides the first in-space demonstration of a millimeter-wave radiometer based on a 35-nm indium phosphide (InP) high-electron-mobility transistor (HEMT) low-noise amplifier (LNA) front end for Earth Science measurements.

The success criterion for TEMPEST-D instrument is to demonstrate cross-calibration between the TEMPEST-D millimeter-wave radiometer and other well-calibrated operational radiometers with similar channels [e.g., the Microwave Humidity Sounder (MHS) operating on NOAA and European MetOp satellites, and the NASA Global Precipitation Measurement (GPM) Microwave Imager (GMI)] with better than 2-K precision and 4-K accuracy.

The TEMPEST-D began in August 2015 as a partnership among Colorado State University (CSU), Fort Collins, CO, USA; Jet Propulsion Laboratory (JPL), Pasadena, CA, USA; and Blue Canyon Technologies (BCT), Boulder, CO, USA. The TEMPEST-D flight instrument was developed and fabricated at JPL and delivered to the CubeSat vendor, BCT. BCT performed the integration of the instrument into their 6U CubeSat bus as well as the flight acceptance testing of the complete flight system, with technical support from JPL. BCT delivered a complete 6U CubeSat flight system with integrated payload to NanoRacks for launch integration on March 22, 2018. The NASA CubeSat Launch Initiative (CSLI) provided launch services for the TEMPEST-D CubeSat. TEMPEST-D was launched by Orbital ATK on CRS-9 from NASA Wallops to the International Space Station (ISS) on May 21, 2018. The TEMPEST-D spacecraft was deployed into an orbit of 410-km altitude and 51.6° inclination by NanoRacks on July 13, 2018.

II. Instrument Architecture

The TEMPEST-D instrument receivers are based on 35-nm InP HEMT LNAs developed jointly by JPL and the Northrop Grumman Corporation [3], Redondo Beach, CA, USA. The reflector scanning and calibration methodology was

Manuscript received May 8, 2020; revised October 9, 2020; accepted November 19, 2020. This work was supported in part by the U.S. National Aeronautics and Space Administration, Science Mission Directorate under Grant NNX15AP56G and Grant 80NSSC20K1124. *(Corresponding author: Sharmila Padmanabhan.)*

Sharmila Padmanabhan is with the Jet Propulsion Laboratory, California Institute of Technology, Pasadena, CA 91109 USA (e-mail: sharmila.padmanabhan@jpl.nasa.gov).

Todd C. Gaier, Alan B. Tanner, Shannon T. Brown, Boon H. Lim, Robert Stachnik, Rudi Bendig, and Richard Cofield are with the NASA/Jet Propulsion Laboratory, California Institute of Technology, Pasadena, CA 91109 USA (e-mail: todd.c.gaier@jpl.nasa.gov; alan.b.tanner@jpl.nasa.gov; shannon.t.brown@jpl.nasa.gov; boon.h.lim@jpl.nasa.gov; robert.a.stachnik@jpl.nasa.gov; rudi.bendig@jpl.nasa.gov; richard.cofield@jpl.nasa.gov).

Steven C. Reising is with the Microwave Systems Laboratory, Colorado State University, Fort Collins, CO 80523 USA (e-mail: steven.reising@colostate.edu).

Color versions of one or more figures in this article are available at https://doi.org/10.1109/TGRS.2020.3041455.

Digital Object Identifier 10.1109/TGRS.2020.3041455

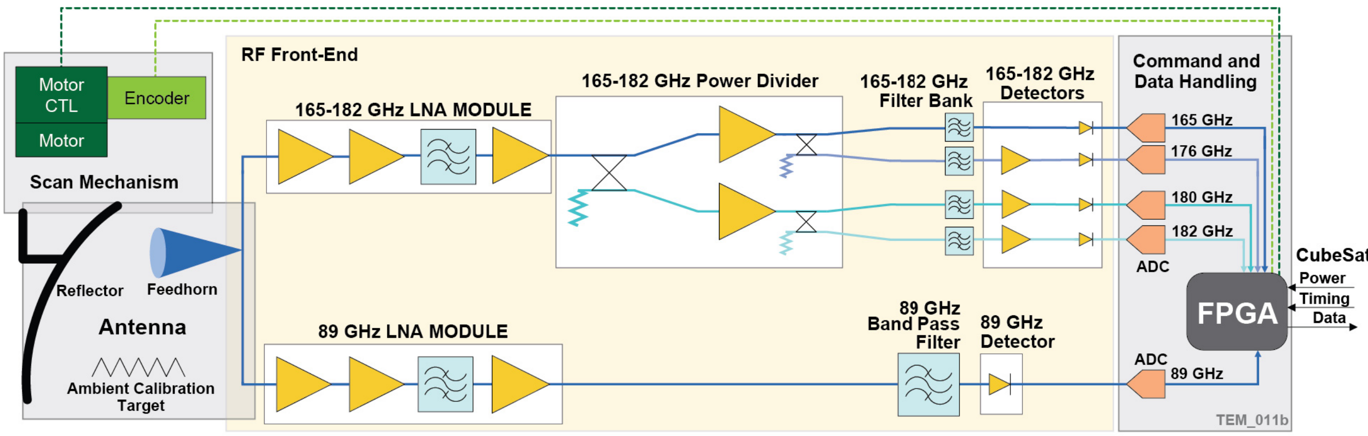

Fig. 1. TEMPEST-D five-frequency millimeter-wave radiometer instrument block diagram.

adapted from the High Altitude MMIC Sounding Radiometer (HAMSR) instrument [4]. The TEMPEST-D instrument block diagram is shown in Fig. 1.

The instrument comprises four major subsystems: antenna, millimeter-wave radiometer, command and data handling (C&DH) electronics, and scan mechanism. The electromagnetic radiation incident upon the instrument enters through an open aperture and is focused onto a dual-frequency feed horn with integrated diplexer by a 90° off-axis paraboloidal scanning reflector antenna [5]. The two waveguide outputs of the feed horn and diplexer are connected to two radio frequency (RF) front-end millimeter-wave LNA modules, the first operating at 87 GHz and the second with four channels from 164 to 181 GHz. At 87 GHz, the signal is amplified, filtered, and detected. From 164 to 181 GHz, the signal is amplified, divided four ways using three 90° hybrid couplers, filtered, and detected. Instrument calibration is achieved by rotating the scanning reflector antenna about the feed horn boresight axis so that the radiometer views both the cosmic microwave background (termed "cold sky" hereafter) and an ambient blackbody calibration target every scan (2 s). The C&DH electronics sample and digitize the detected signals output by the RF front end, as well as control and monitor the operation of the instrument.

The optical subsystem is a compact design consisting of the reflector, dual-frequency feed horn, and ambient calibration target with heritage from multiple sources [HAMSR; Microwave Sounding Unit (MSU), Advanced Microwave Sounding Unit (AMSU), etc.]. The reflector rotates continuously at a rate of 30 r/min to view the Earth, where data are typically stored over the scanning range from $-65°$ to $+65°$ from nadir, followed by observations of cold space and the ambient blackbody calibration target, as shown in Fig. 2. The 10.5 cm $\times$ 7 cm reflector is machined from aluminum and is lightly abraded to provide an optically diffuse surface to avoid issues from direct solar illumination. A single dual-frequency feed horn with integrated diplexer provides coincident beams in all observed millimeter-wave bands (although the 87-GHz polarization is perpendicular to that of the higher frequency channels). The feed horn assembly required machining, gold plating, and stacking of corrugated rings [5]. Fig. 3 shows the antenna components and the calibration target as assembled. By design, the polarization is quasi-vertical for the 87-GHz channel and quasi-horizontal for all the other channels.

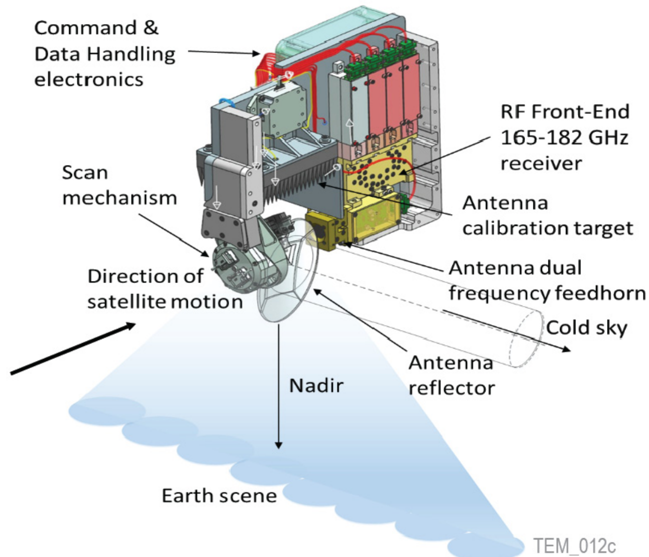

Fig. 2. TEMPEST-D millimeter-wave radiometer instrument scans at 30 r/min to view the Earth scene across a 935-km swath from 400-km orbital altitude.

The antenna half-power beamwidths (HPBWs) are 3.6° at 87 GHz, 1.68° at 164 GHz, 1.69° at 174 GHz, 1.72° at 178 GHz, and 1.8° at 181 GHz. Sidelobes for angles further than 10° off boresight are well below 30 dB, and the main-beam efficiency is greater than 91%, which minimizes footprint contamination. The surface footprint at nadir is 25 km at 87 GHz and 12.5 km at 181 GHz from the nominal orbital altitude of 400 km.

The calibration target is based on the designs for the Microwave Limb Sounder (MLS) and HAMSR [6] and was designed for TEMPEST-D to have greater than 50-dB return loss from 40 to 220 GHz. The target is made of aluminum pyramids coated with ferrite-loaded epoxy-absorbing material. The temperature across the target is measured using three embedded National Institute of Standards and Technology (NIST)-traceable thermistors to quantify the thermal gradients.

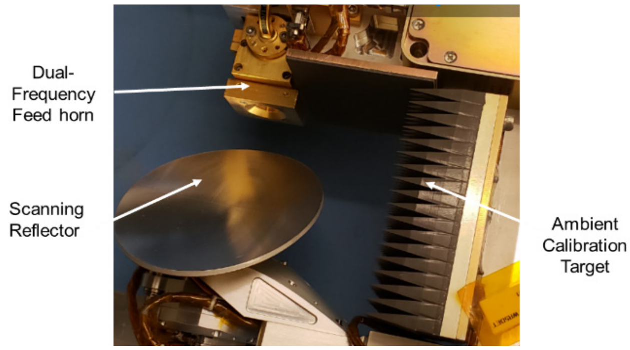

Fig. 3. Antenna components assembled in the instrument.

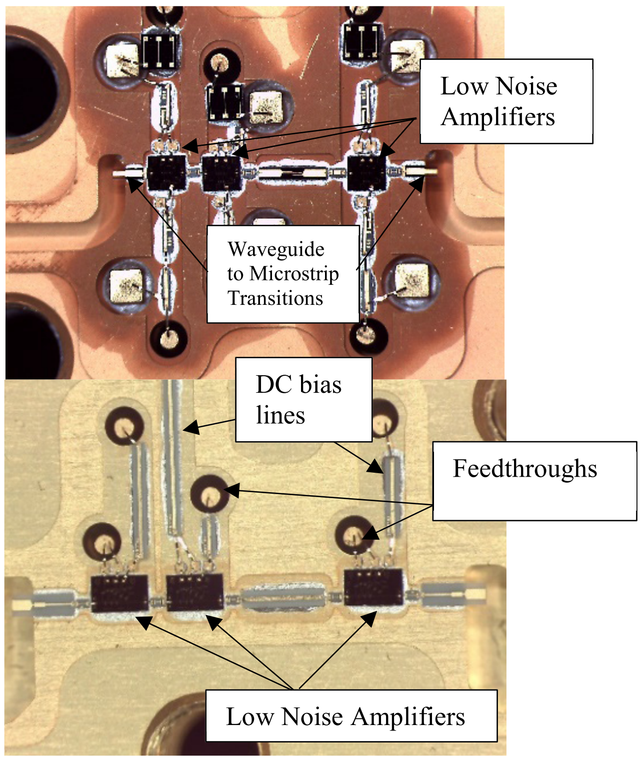

Fig. 4. (Top) 164–181-GHz LNA module. (Bottom) 87-GHz LNA module.

In addition, thermistors are installed in the two RF front-end LNA modules and the power divider block, all of which contain temperature-sensitive amplifiers.

The RF front-end direct-detection radiometers are low power and compact, consisting of LNA modules, a power divider, filters, and detectors. The LNA modules have a low-mass design using a cascade of 35-nm InP HEMT-based LNAs. These modules are gold-plated waveguide modules in which monolithic microwave integrated circuit (MMIC) LNAs and detector diodes are epoxied to the housing using silver epoxy and connected via wire-bonding using gold wire. Fig. 4 provides the photographs of the assembled 164–181-GHz LNA module and the 87-GHz LNA module. JPL used previously designed 35-nm InP MMIC LNAs from Northrop Grumman's process for both LNA modules [3]. These LNAs have been measured in a packaged MMIC-based receiver to have a noise temperature of 350 K (3.4 dB) near 183 GHz at room temperature with a gain of ∼17 dB.

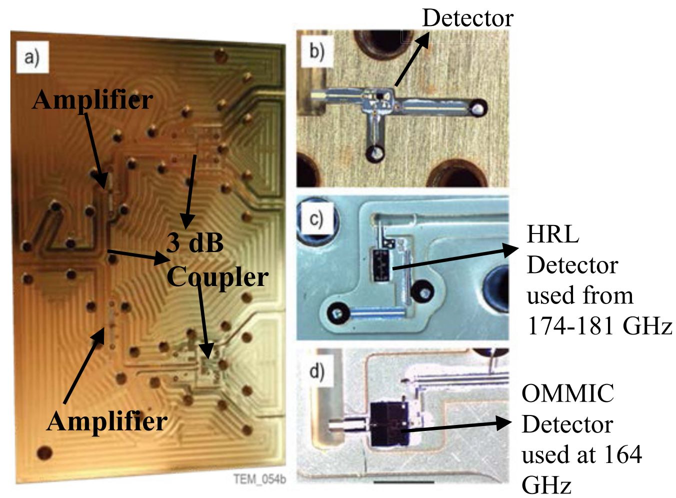

Fig. 5. (a) RF front-end power divider module. (b) 87-GHz detector. (c) and (d) 164–181-GHz detectors.

Each amplifier consumes 30 mW of power, and the technology has been tested across a wide range of temperatures and in vacuum [7]. The detection bandwidths are defined using waveguide-based bandpass filters. The amplified and filtered 87-GHz signal is detected by a commercially available zero-bias Keysight gallium arsenide (GaAs) Schottky detector diode [8] packaged in a gold-plated waveguide module machined in aluminum. The 164–181-GHz channels are separated using a 4:1 power divider [Fig. 5(a)] and defined by waveguide bandpass filters. The 164–181-GHz detectors were assembled at JPL using tunnel diodes from HRL Laboratories LLC, Malibu, CA, USA [9] and OMMIC, Limeil-Brévannes, France [10]. All modules include small printed wiring assemblies (PWAs) to regulate the bias voltages and currents to the InP MMIC LNAs and to amplify the detected output signal to a nominal 1 V (with a gain of 900) using OP270 operational amplifiers.

The C&DH circuit includes 18-bit analog-to-digital converters (ADCs) for digitizing the radiometer output channels and the Microsemi ProASIC3L field-programmable gate array (FPGA) for packetizing the data and transferring it to the spacecraft computer using UART LVDS. A 12-bit, 8-channel ADC digitizes the thermistor voltages, which provide the temperatures of the instrument subsystems. JPL performed radiation analysis for components that were susceptible to single event latchup, such as the encoder on the scanning motor and ADC for TEMPEST-D. TEMPEST-D used commercially available off-the-shelf (COTS) parts with the exception of a few radiation tolerant devices that were purchased as space-qualified components (e.g., clock and voltage regulators). The C&DH PWA was assembled into the machined housing, as shown in Fig. 6.

The TEMPEST scan mechanism was developed by BCT. The BCT motor was modified from their reaction wheel product line, which had previously been demonstrated on-orbit for more than 200 million revolutions (the TEMPEST-D scan mechanism had demonstrated more than 10 million revolutions as of May 1, 2019). Hall effect sensors are used to

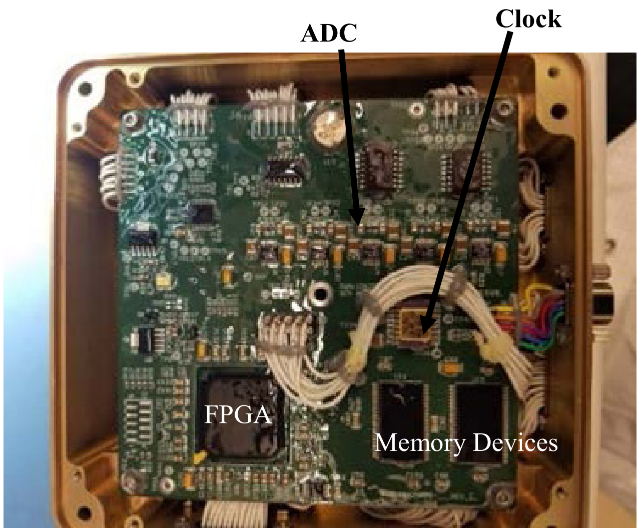

Fig. 6. Photograph of the TEMPEST-D electronics chassis housing and the C&DH PWA.

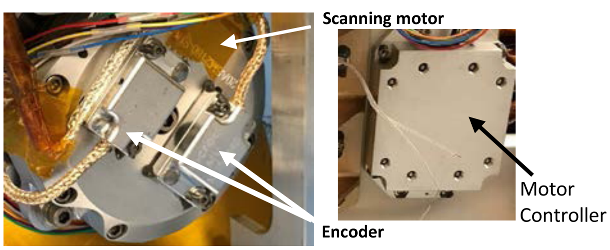

Fig. 7. TEMPEST-D scan mechanism components showing the (Left) two redundant encoders and the (Right) motor controller chassis.

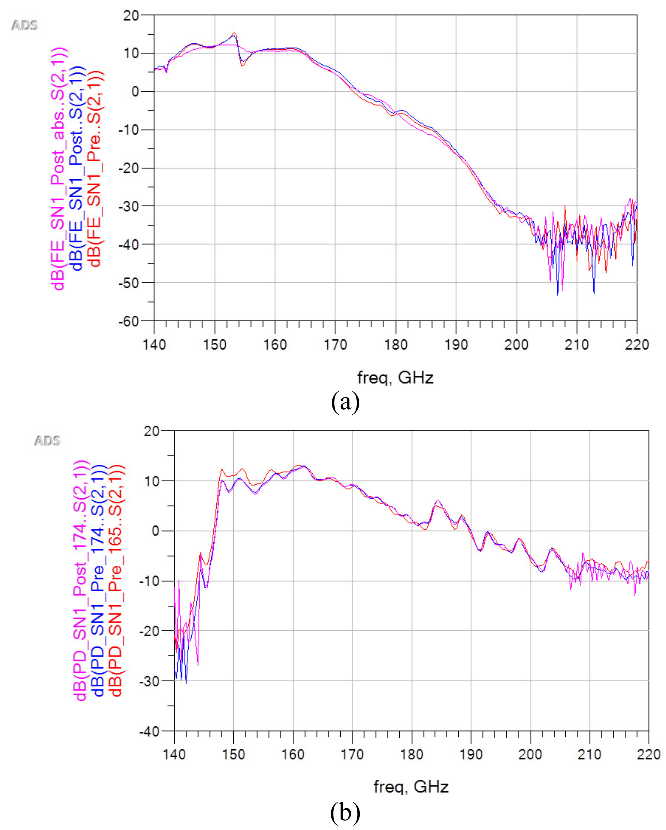

Fig. 8. Comparison of pre- and post-burn-in gain (S_{21}) for 164–181 GHz. (a) RF front-end module. (b) Power divider module. Pre-burn-in is shown in red, as compared with post-burn-in shown in blue and post-burn-in with absorber inserted to remove any cavity effects shown in magenta.

switch the current in the motor phases to generate motion. Two encoders are integrated into the scan mechanism for redundancy. The Mercury 1500-V output digital vacuum rotary encoder is manufactured by Celera Motion and is configured for a resolution of 16 364 counts per revolution. The motor controller uses a single reaction wheel driver circuit based on an ATMEL microcontroller. The scanning mechanism was vibrated and thermal-vacuum (TVAC) tested prelaunch, and is currently operational on-orbit in the TEMPEST-D Instrument. Fig. 7 shows the TEMPEST-D scan mechanism components.

III. Instrument Assembly

The instrument assembly began with screening and selecting the best LNAs by using wafer-probed measurements of the S-parameters. The technical criteria for picking LNAs were values of gate voltage, drain and gate currents, as well as S_{21} to provide >15-dB gain across the band in addition to input and output return loss below 5 dB across the band. The prescreening of the spectral performance, including checking the input and output return loss and their variation as a function of bias voltage, made it possible to obtain an unconditionally stable configuration with the addition of attenuation at the output of the amplifiers. The amplifier will not oscillate due to the presence of the attenuators at the source and load. This was followed by installing the amplifiers into the gold-plated aluminum housings using conductive silver epoxy. With all components installed, the amplifier, power divider, and detector modules were subjected to burn-in testing with devices biased at nominal operating currents and heated to 110 °C for 100 h to thermally accelerate the infant mortality of the MMIC devices. Infant mortality could result in instability or degraded performance as a drop in gain or change in bias conditions.

S-parameter measurements of the amplifier modules pre- and post-burn-in testing verified the performance of the MMIC devices. Amplifier modules include attenuators at the output of the amplifier and other losses from waveguide to microstrip transitions as well as any filtering. Fig. 8 shows the gain performance (S_{21}) of the 164–181-GHz RF front-end and power divider module before and after burn-in testing. The 87-GHz channel showed similar match in gain performance before and after burn-in.

After completion of burn-in, the power divider module and the filter modules were integrated, and S-parameters were measured, as shown in Fig. 9. All modules were then integrated and tested as a radiometer by measuring detected voltages using the preamplifier/digitizer to generate radiometric counts sampled every 5 ms, which were then packetized and transmitted to the spacecraft simulator. Fig. 10 provides a photograph of the integrated radiometer as integrated into the 6U CubeSat spacecraft.

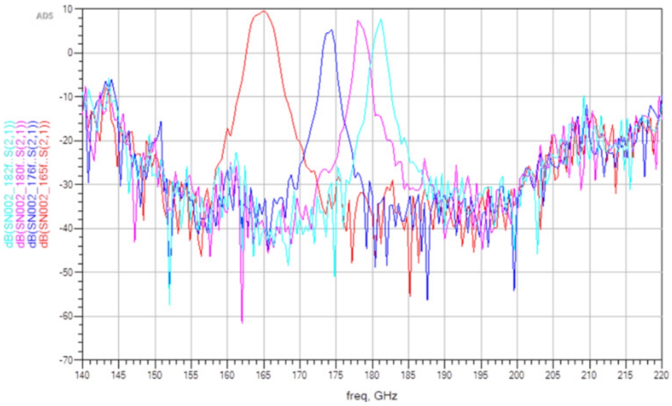

Fig. 9. Measured S-parameters for power divider combined with the filters.

IV. Prelaunch Characterization

A full set of prelaunch calibration and characterization testing was performed on the TEMPEST-D instrument, including measurements of radiometric response, spectral response, linearity, and antenna pattern characterization.

A. End-to-End Spectral Response

The response of the predetection filter is typically assumed to be the spectral response for radiometer systems [11]. For TEMPEST-D, the individual filter response for each channel was measured by performing a two-port S-parameter measurement. However, this measurement does not account for the impact of the spectral response of LNAs and other devices that constitute the end-to-end radiometer system. This is especially true for the direct-detection architecture in which detection is at the input RF instead of at the traditional intermediate frequency (IF). The end-to-end spectral response of TEMPEST-D was measured by using a vector network analyzer with frequency extension modules as a source (separately calibrated) to transmit a continuous wave (CW) with frequency swept over the 160–185-GHz range. Each frequency was active for 20 s, controlled by a computer script. For final bandpass measurement, this CW signal was incident upon the TEMPEST-D radiometer antenna optics from the far field, and the radiometric counts were measured with the CW signal modulated ON and OFF during the frequency sweep. The spectral response was calibrated by measuring the CW signal output by the frequency extension module using an Erickson PM5 power meter. Each end-to-end spectral response is plotted, along with the corresponding individual filter response of the predetection filter installed in each channel, in Figs. 11–15. In Figs. 11–15, it is evident that the end-to-end spectral response is substantially different from the filter response, resulting from gain variations with frequency and standing waves in the system.

B. Linearity Measurement

The instrument linearity was measured separately for the 87- and 164–181-GHz channels. To measure the system linearity, the input signal viewed by the feed horn is switched between an absorber at ambient temperature and another absorber cooled using liquid nitrogen. A coupler with a warm noise source (implemented using an LNA with a matched input termination) is used to measure a small noise source deflection of ~100 K. A function generator is used to switch the LNA bias ON and OFF at 1 Hz, providing a noise source "ON" for 100 samples and "OFF" for 100 samples, consecutively. A block diagram of the test setup is illustrated in Fig. 16(a). The noise source deflection for an ambient input at ~290 K is compared with the deflection at a liquid nitrogen cooled absorber input at ~80 K that is used to calculate the percent linearity for each channel over the 80–290-K dynamic range of the measurement. Fig. 16(b) shows the radiometric counts measured for the 178-GHz channel during the linearity measurement. The nonlinearity is calculated as

$$\frac{\text{WarmTargetNSDeflection} - \text{ColdTargetNSDeflection}}{\text{WarmTargetNSDeflection}} \times 100$$

where

$$\begin{aligned}\text{WarmTargetNSDeflection} &= \text{WarmtargetNSon}\\ &\quad - \text{WarmtargetNSoff}\\ \text{ColdTargetNSDeflection} &= \text{ColdtargetNSon}\\ &\quad - \text{ColdtargetNSoff}.\end{aligned}$$

The nonlinearity for all channels is tabulated in Table I.

TABLE I
Maximum Measured Nonlinearity

Channel	Non-Linearity (%)
89	0.3
164	2.9
174	2.1
178	2.9
181	2.7

C. Antenna Pattern Characterization

Several measurements were performed to validate the modeled antenna patterns to characterize the sidelobes and to determine any scan-dependent bias. For all of these measurements, the radiometer was integrated in a spare 6U CubeSat spacecraft chassis without solar panels.

1) Model Validation: The TEMPEST-D radiometer main-lobe antenna patterns were measured in the laboratory, as shown in Fig. 17. Azimuth angles were manually stepped in 0.25° increments as the radiometer operated and scanned in elevation. The radiometer measured a signal source consisting of a CW oscillator that was stepped through the various frequencies. Each frequency was active for 20 s, under controlled by a script. The antenna rotated in elevation at 30 r/min or 180° per second. The TEMPEST-D radiometer sample rate is 200 Hz, and each sample represents an effective integration period of 5 ms, achieved using a combination of numerical integration and analog low-pass filtering of the postdetection video signal. This integration time and scan rate

This article has been accepted for inclusion in a future issue of this journal. Content is final as presented, with the exception of pagination.

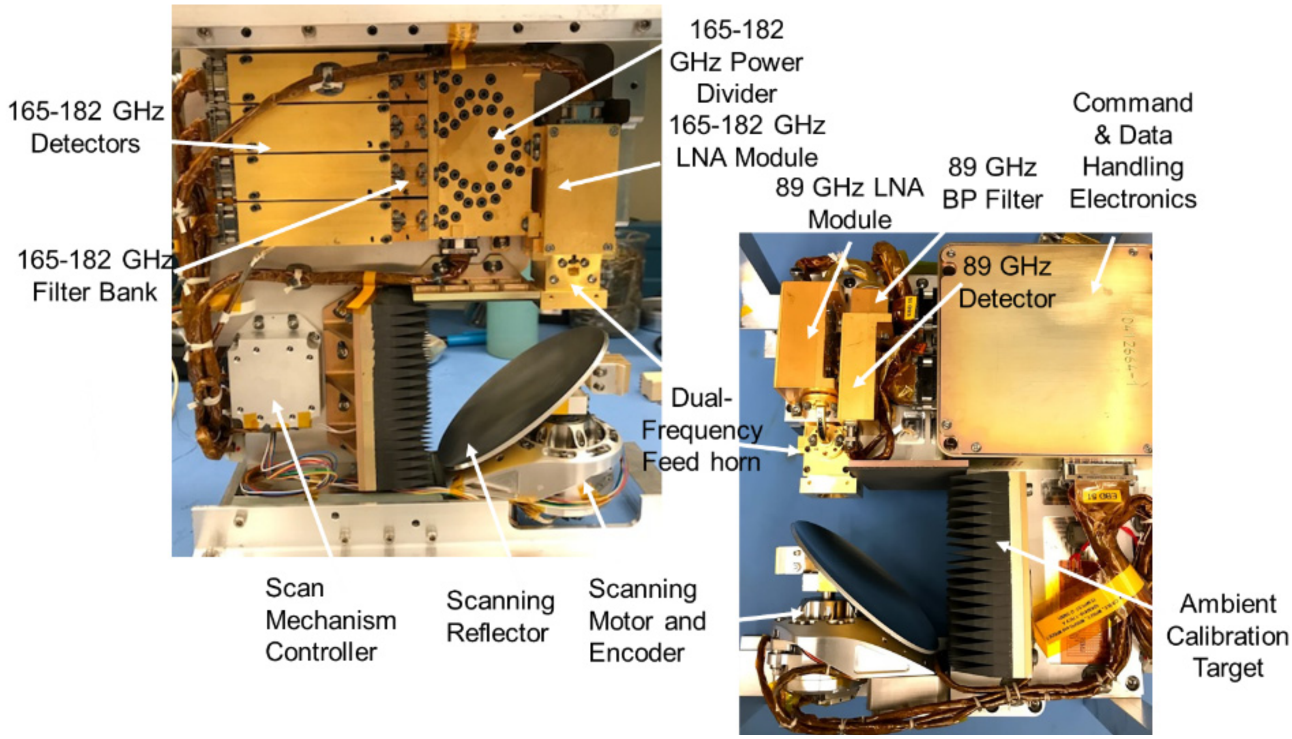

Fig. 10. TEMPEST-D radiometer as packaged and integrated into the 6U CubeSat spacecraft.

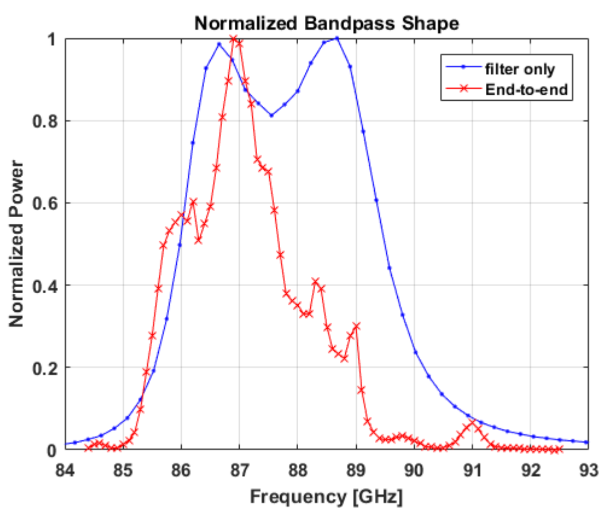

Fig. 11. End-to-end spectral response for 87-GHz channel in red compared with the filter response in blue.

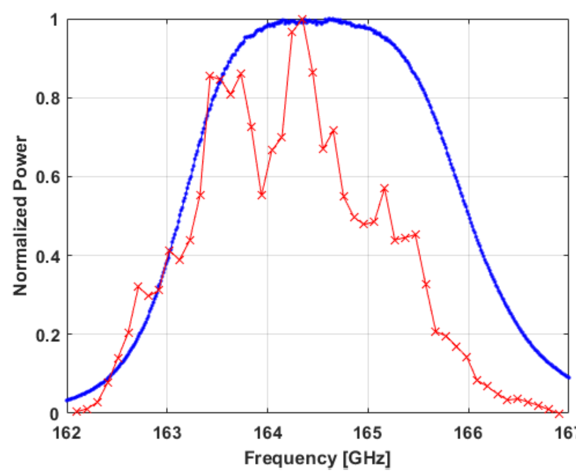

Fig. 12. End-to-end spectral response for 164-GHz channel in red compared with the filter response in blue.

result in a slight "smearing" of the antenna beam pattern as the elevation axis spins, which will be modeled below. The range between the source and the radiometer was 5 m. Scan directions are noted in the caption of Fig. 17. Because these measurements focused only on the shape of the main lobe of the beam, the azimuth range was small: between about $-3°$ and $+3°$ of azimuth angle about the beam center. The flight instrument on-orbit is called FM1, and the flight spare instrument is called FM2.

Source power levels for the WR5 and WR10 sources were heavily attenuated using two vane attenuators each. The source feed horns for both tests were 25-dBi gain pyramidal horns. These horns kept the signal energy close to the instrument so that multipath reflections in the laboratory were manageable. It was discovered during these tests that the large attenuators and very low signal levels rendered the measurements vulnerable to leakage from the back of the multiplier sources used in the RF sources for the antenna pattern measurement. Such leakage could scatter around the laboratory in a manner, impacting some of the measurements. This leakage path was successfully attenuated for the WR5 head by placing absorber around the source antenna.

All radiometric data were normalized by the average of reference target counts immediately before and after each

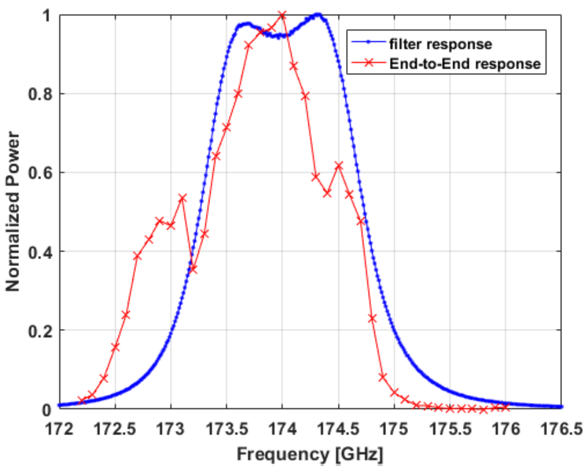

Fig. 13. End-to-end spectral response for 174-GHz channel in red compared with the filter response in blue.

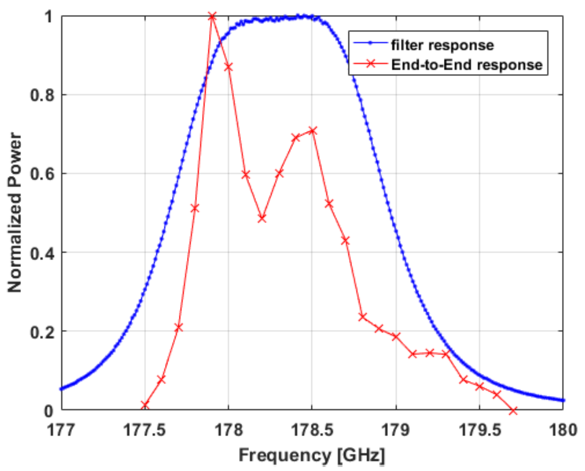

Fig. 14. End-to-end spectral response for 178-GHz channel in red compared with the filter response in blue.

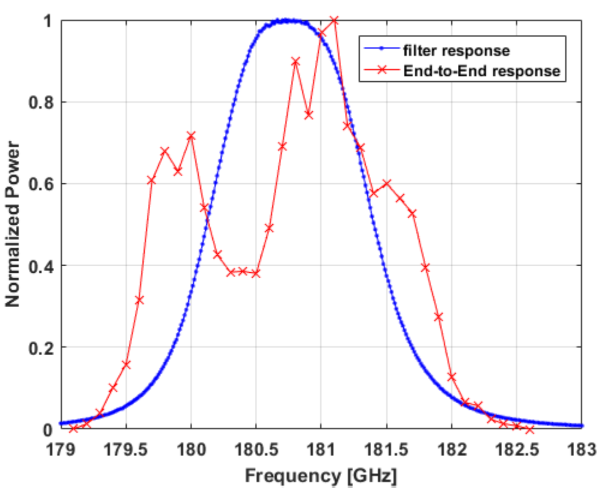

Fig. 15. End-to-end spectral response for 181-GHz channel in red compared with the filter response in blue.

antenna scan (i.e., normalized counts = counts/reference counts). To the extent that the receiver noise temperatures and ambient target temperatures are stable (within the 2-s scan period and 20-s measurement time at a specific frequency), this step stabilizes all measurements with respect to gain fluctuations. Data were sorted by source frequency, azimuth position, and elevation. At each position and frequency, data with the source switched OFF were subtracted from data with the source switched ON to produce a foreground minus background "deflection." This step removes the background signal to yield the source response as a fraction of ambient system noise temperature. Using 2-D interpolation, data were regridded to 0.1° azimuth and elevation samples.

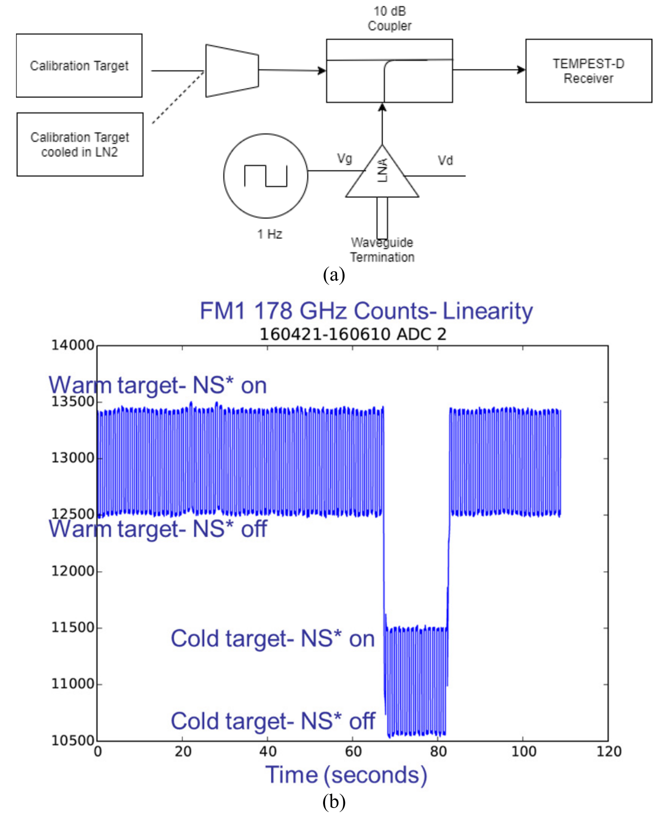

Fig. 16. (a) Block diagram of the linearity test setup. (b) Linearity measurements for 178-GHz channel showing noise source turning on and off while viewing both warm and cold target at the input.

Numerical model predictions of the antenna patterns at frequencies of 183 and 92 GHz were extrapolated to compare with measured patterns at the operating frequency channels from 87 to 181 GHz.

Fig. 18 provides a comparison of the results with the model antenna pattern. There is very good match of measurements in all bands with the model in the elevation cuts, and good match in some of the channels versus azimuth. Overall, the measured -3-dB beamwidths are between 0° and 0.2° wider than the model patterns in azimuth, and very nearly matched in elevation. In addition, the flight and flight spare units are also well matched.

2) Impact of Spacecraft Chassis: The 164–181-GHz antenna patterns are measured by placing the instrument inside of the spacecraft chassis. During these tests, care was taken to note orientation and alignment. This position was aligned with an estimated error of ±0.1°. The main-beam antenna patterns

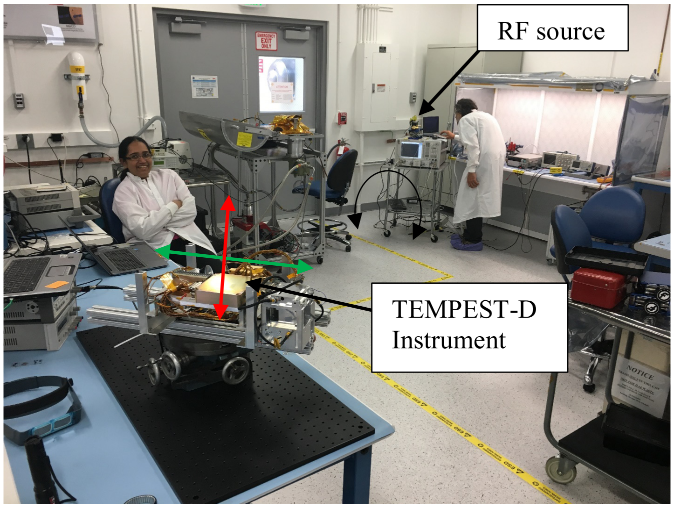

Fig. 17. Test configuration for antenna pattern characterization. Elevation scans shown by the red arrow were performed by the radiometer antenna scan mechanism, which rotated in a direction from the floor of the lab, upward past the source at an encoder angle of about 41°, then along the ceiling and back toward the calibration target. Negative azimuth angles (green arrow) start with the instrument pointed to the right of the source (such that the source was to the left of the radiometer beam).

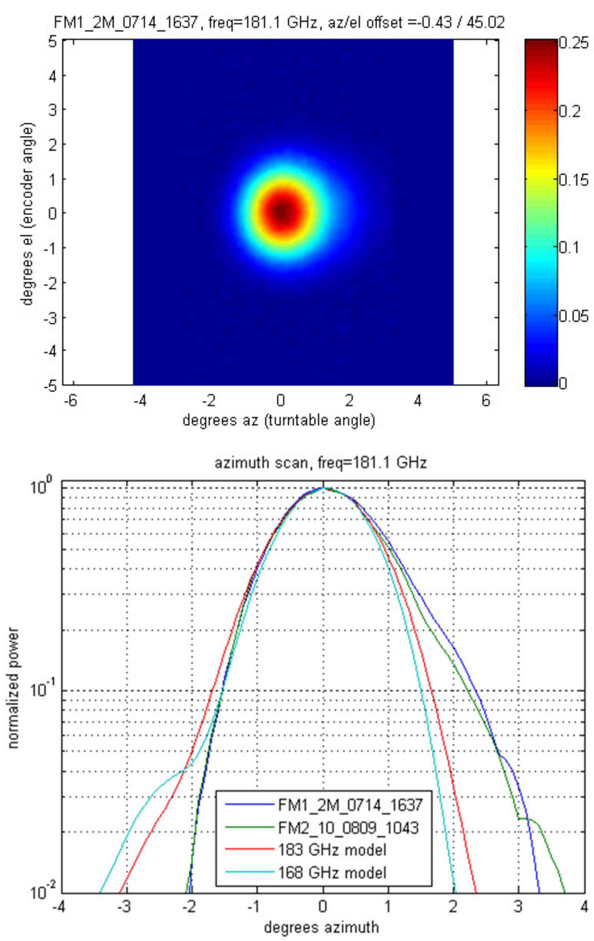

Fig. 18. Comparison of measured antenna patterns for both the flight (FM1) and flight spare (FM2) instruments with the modeled patterns.

measured with and without spacecraft are identical (as shown in Fig. 19), clearly showing no impact from the spacecraft chassis.

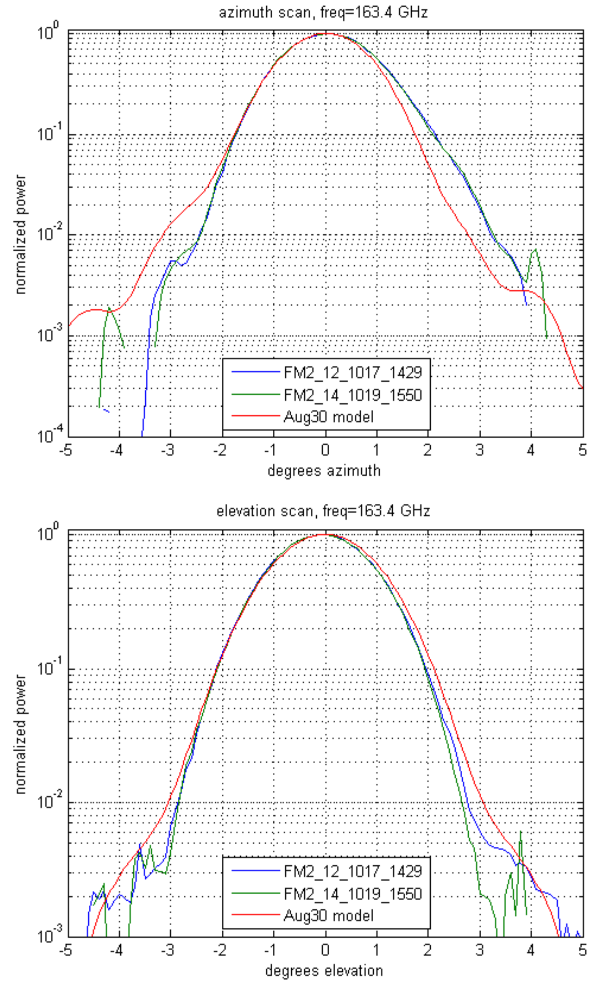

Fig. 19. Identical azimuth and elevation scans for the flight spare instrument measured with and without the spacecraft chassis.

D. Rooftop Tests

Rooftop measurements of the flight spare instrument were performed, in addition to far sidelobe tests, using a source on another roof 100 m away. The instrument was also placed in various orientations in which the instrument was covered with an absorber to mask the sky. The purpose of these tests is to determine whether far sidelobes of the antenna can corrupt brightness temperatures, and if so, to what magnitude.

Fig. 20 illustrates some of the rooftop testing performed to characterize the sidelobe contributions. The masked/unmasked data are plotted in black and red, respectively.

As a primary result of the rooftop test, Fig. 21 shows that there is no discernible bias of nadir observed brightness temperatures due to masks above the instrument. In these plots, the black curve is brightness when a mask is applied (absorber panel held above the instrument); the nearly matching red curves represent the unmasked brightness before and after the test. This provides good evidence that the far sidelobes are largely contained below the horizon.

Finally, Fig. 22 shows how the sky temperatures measured when the instrument viewed the sky in the "nadir up" (the same as Earth view aperture pointing up) orientation compared with the space view aperture (left side) pointed up.

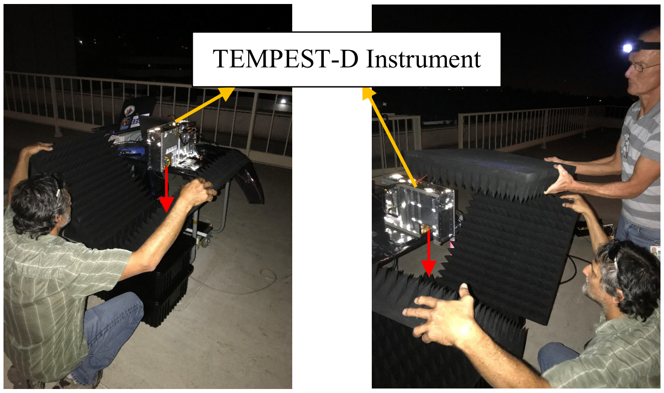

Fig. 20. "Nadir down (ND)" orientation shown by red arrow, with TEMPEST-D pointed down into the absorbers shown. The three absorbers were held in this position throughout all the "ND" observations, while the sky mask was applied—in this example "right sky mask."

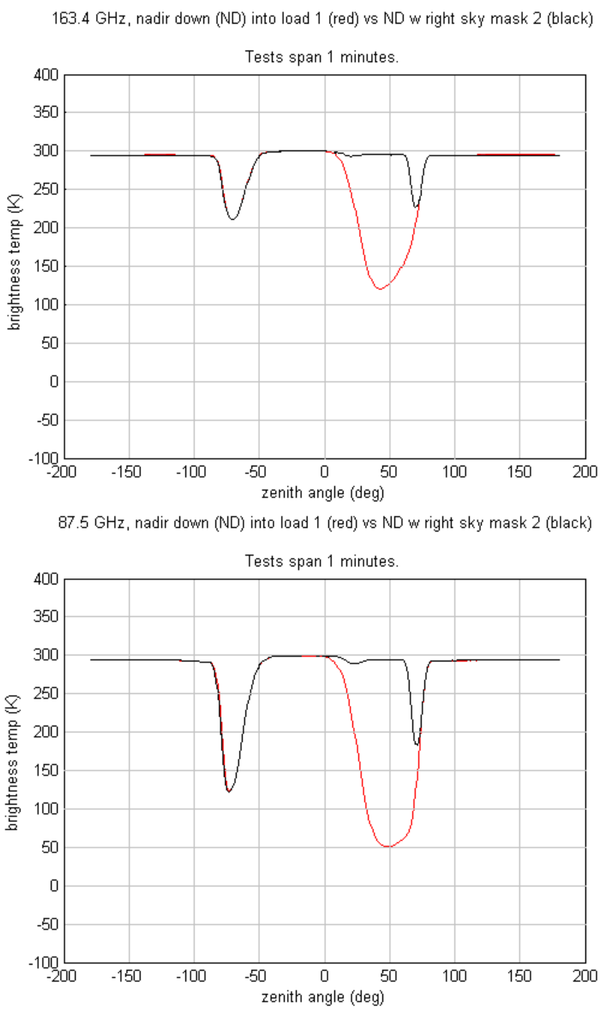

Fig. 21. Observed brightness temperatures at (Top) 163 and (Bottom) 87 GHz.

The zenith-mapped brightness temperatures are compared between the Earth view pointed up (black solid) and the space view aperture pointed up (red solid). The actual measured data are shown in black dashed and red dashed for the Earth view

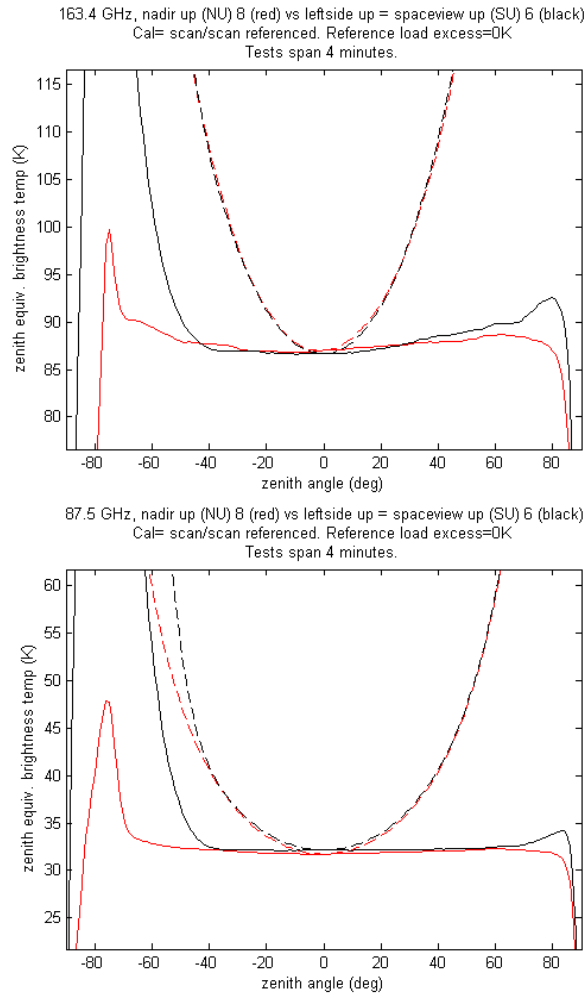

Fig. 22. Comparison of sky brightness temperatures at (Top) 163 and (Bottom) 87 GHz observed when the instrument was oriented either nadir-up (red) or with the space view port up (black). Zenith-mapped brightness temperatures (solid traces) show very good agreement here, as do the actual measured brightness temperatures (dashed).

aperture pointing up and the space view pointing up, respectively. These data further confirm that the scan-dependent biases are small. These results were subsequently confirmed on-orbit through spacecraft calibration maneuvers [12].

E. TVAC Testing

Instrument performance was characterized in a TVAC environment from −25 °C to +60 °C (over three complete cycles) with both hot and cold instrument power starts. The gain and noise-equivalent differential temperature (NEDT) were derived for all channels by using the ambient target as well as a calibration target cooled by the chamber cold finger to ∼150 K and a fixed temperature target on the lid of the chamber. Fig. 23 shows the measured gain and NEDT of all channels as a function of instrument temperature. The radiometric target brightness temperatures for the 87-GHz channel are shown in Fig. 24 as a function of scan angle.

F. Vibration Testing

The TEMPEST-D instrument was subjected to NASA GEVS [13] level random vibration testing in three orthogonal

This article has been accepted for inclusion in a future issue of this journal. Content is final as presented, with the exception of pagination.

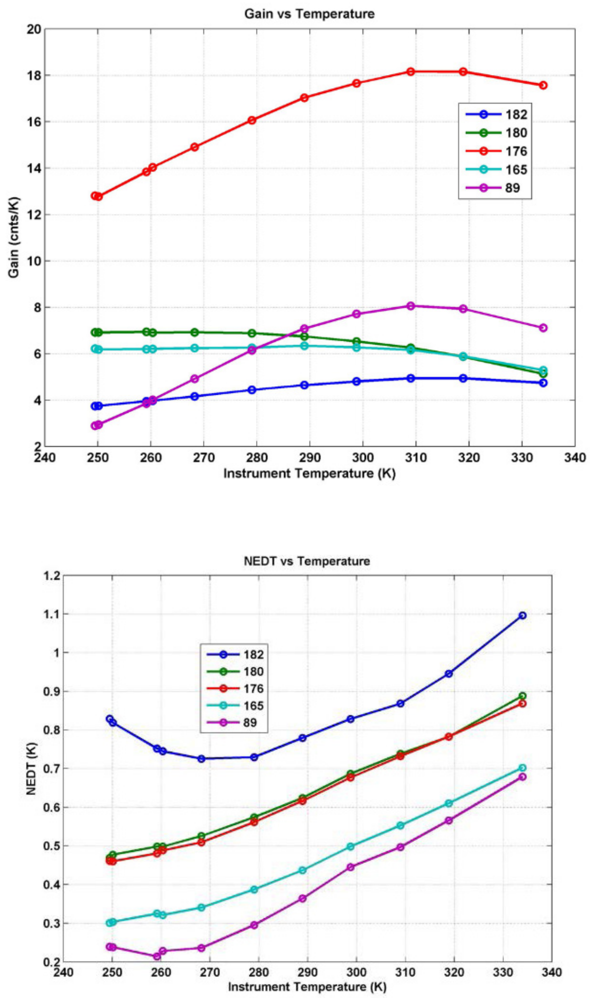

Fig. 23. (Top) Measured gain and (Bottom) NEDT testing results of the TEMPEST-D instrument in the TVAC chamber at JPL.

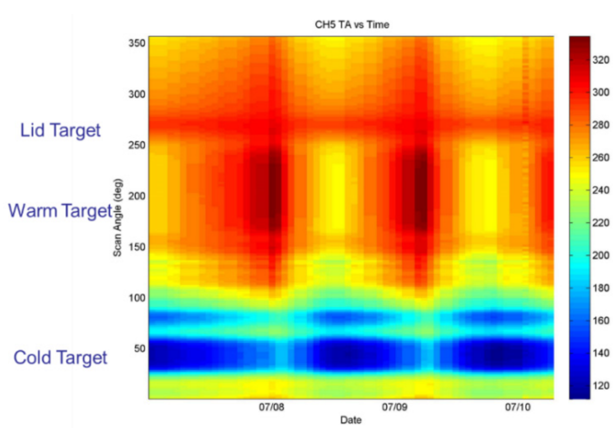

Fig. 24. Radiometric brightness temperatures for the TEMPEST-D 87-GHz channel in the TVAC chamber.

axes. The objective of the random vibration test is to validate TEMPEST-D design for random vibration environments expected during system testing, launch, and workmanship. Full-level random vibration test run inputs are documented in Table II. Spectral limits were calculated, and force limits

TABLE II
TEMPEST-D Random Vibration Input

Axis	Frequency, Hz	Qualification Level
X, Y, Z	20 50-800 2000 Overall	0.026 g^2/Hz 0.16 g^2/Hz 0.026 g^2/Hz 14.1 G_{rms}

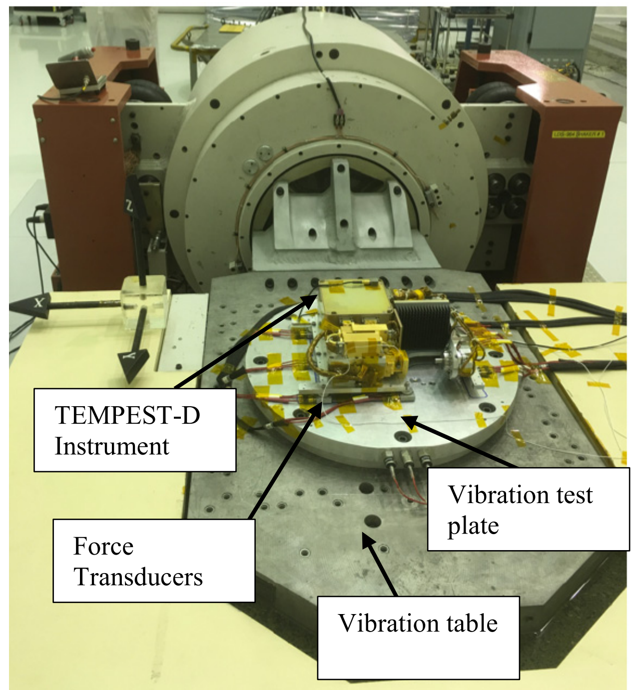

Fig. 25. TEMPEST-D proto-flight-level random vibration test setup for the y-axis.

were calculated for each axis. Test instrumentation consisted of two control accelerometers. A monitor accelerometer was located near one of the control accelerometers to verify the input levels. Force transducers were installed between the vibration test fixture and TEMPEST-D instrument (one for each mounting bolt), oriented parallel to the unit coordinate axes. The vibration response of the TEMPEST-D was measured by four triaxial accelerometers. Fig. 25 shows the y-axis vibration test setup.

Radiometric testing was performed previbration and postvibration test to verify that radiometric performance was unchanged. There was less than 0.5% of gain change observed in all channels.

G. Spacecraft Integration and Testing

The instrument was integrated into the 6U CubeSat at BCT in Boulder, CO. Multiple bench-top tests were performed to verify instrument performance. In addition, staring at the internal calibration target provided measurement noise as well as characterization of any electromagnetic self-compatibility issues with the spacecraft. About four months before the flight instrument was ready for delivery, the flight spare instrument

This article has been accepted for inclusion in a future issue of this journal. Content is final as presented, with the exception of pagination.

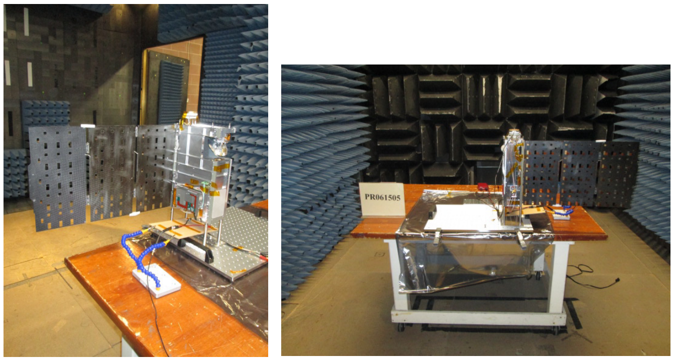

Fig. 26. Self-compatibility test setup with flight spare instrument integrated in flight CubeSat bus.

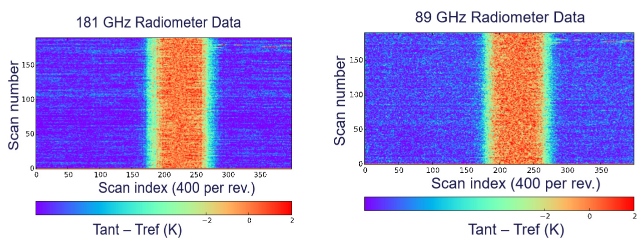

Fig. 27. Self-compatibility test measurements for the (Left) 181-GHz channel and (Right) 87-GHz channel.

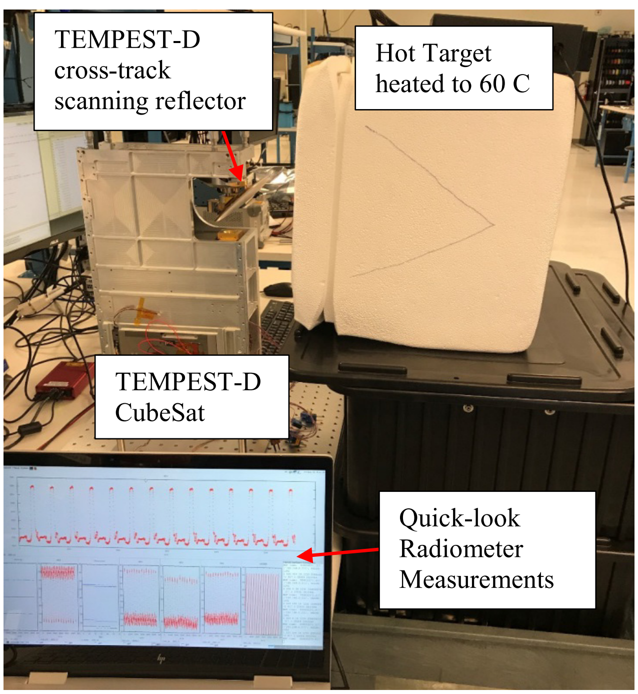

Fig. 28. TEMPEST-D on the bench performing radiometric calibration at BCT.

was delivered to verify that interfaces and grounding as well as characterization of any electromagnetic self-compatibility issues with the spacecraft. For these tests, the flight spare was electrically integrated with the flight CubeSat bus on the bench at BCT.

1) Compatibility Testing With Flight-Spare Instrument: Compatibility testing was performed in the anechoic chamber

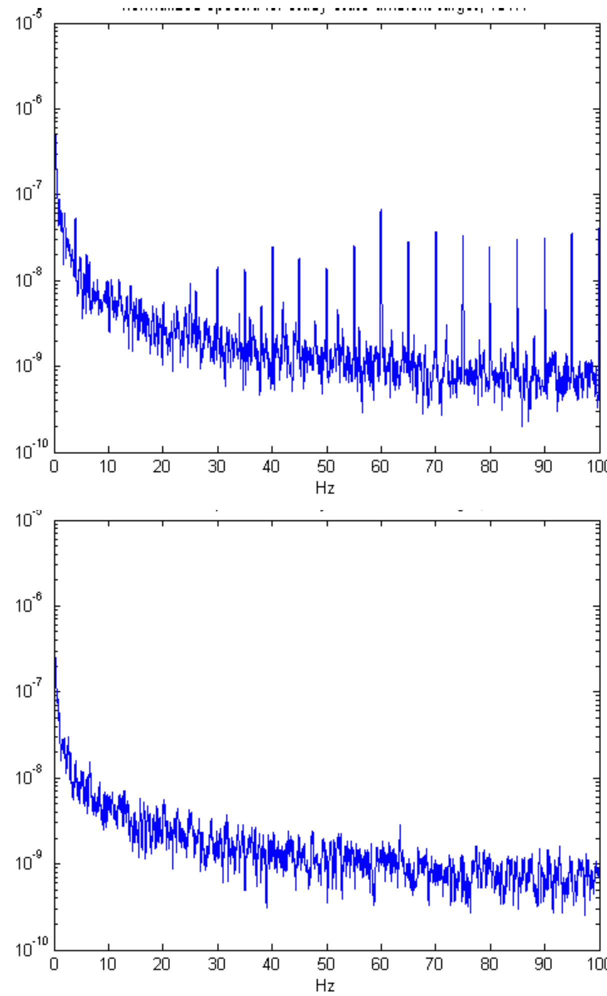

Fig. 29. Normalized spectra measured while viewing a steady-state internal ambient calibration target. (Top) 181 GHz. (Bottom) 178 GHz.

(as shown in Fig. 26) to assess any issues with the CubeSat avionics interfering with the radiometric data and vice versa. This early test uncovered I^2C interface anomalies in the CubeSat bus and helped to mitigate these issues before the actual flight instrument unit arrived for the integration with the flight CubeSat bus. The instrument measurements were analyzed and looked clean, as is evident in the maps of the differences of the antenna temperature (TA) from the hot target temperature plotted for each sample (x-axis) in the scan over multiple scans (y-axis) in Fig. 27.

2) Flight System TVAC Testing: After integration of the flight instrument with the flight spacecraft, several bench top tests were performed to measure gain and NEDT and also check for any electromagnetic compatibility issues with the CubeSat avionics.

Fig. 28 shows the bench top test setup for TEMPEST-D viewing an external calibration target heated to 65 °C with a real-time data viewer. This target proved useful for monitoring the health of the instrument during integration and test (I&T). The normalized data were evaluated for noise by calculating the standard deviation among several consecutive antenna scans at each of the scan positions. For the most part, the noise levels were as expected. Fig. 29 compares the normalized

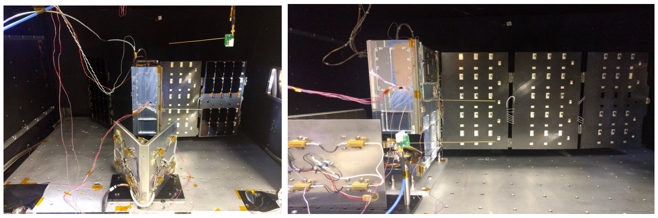

Fig. 30. TEMPEST-D setup in TVAC chamber with the hot target for radiometric calibration.

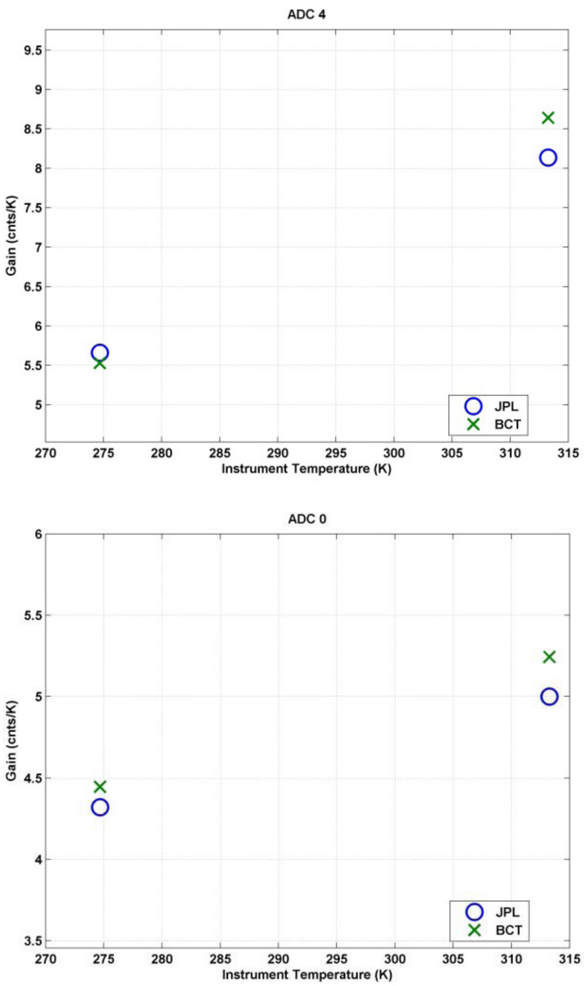

Fig. 31. Gain measurements during JPL instrument-only TVAC test versus BCT spacecraft-level TVAC test for (Top) 87 and (Bottom) 181 GHz.

spectra for 181 GHz versus 178 GHz for measurements viewing the steady-state internal ambient target. The 181-GHz channel shows additional spurious digital noise when viewing a steady-state ambient target. This noise could be caused by parts variability in the ADC circuit and did not appear in other channels at this level. Also, this noise level would not affect calibrated TA measurements and was small enough to meet the success criteria for the mission.

Fig. 30 shows the setup of the TEMPEST-D Spacecraft inside the TVAC chamber. The gain computed during the final TVAC test using the external hot target and internal ambient target was compared with the end-to-end gain measured for the JPL instrument-only TVAC test, as shown in Fig. 31. The NEDT values computed for the all of the channels during the spacecraft-level TVAC test are shown in Fig. 32.

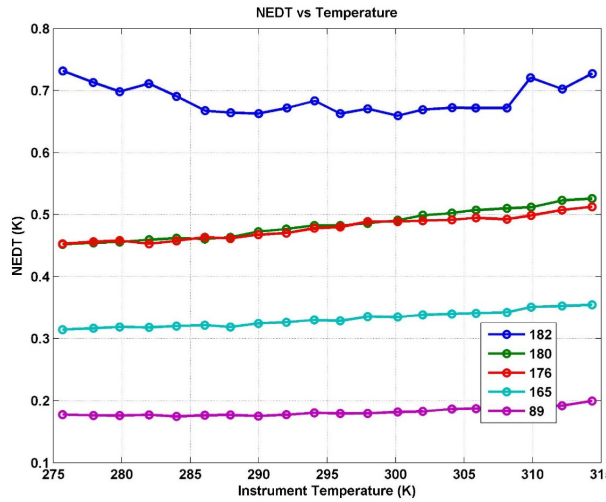

Fig. 32. NEDT measurements as a function of instrument temperature for all channels during spacecraft-level TVAC test.

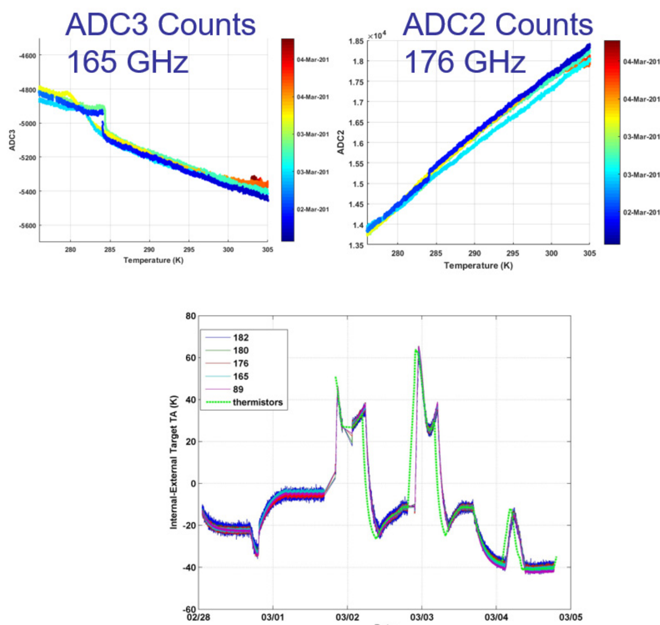

Fig. 33. Radiometric count jumps for the (Top left and right, respectively) 164- and 174-GHz channels as a function of the physical temperatures of the calibration target measured by the thermistors. (Bottom) Calibrated TA as a function of time. There is a lag observed between thermistor measurement and the radiometric brightness, as expected.

The final thermal cycle during the TVAC testing at the CubeSat level showed a gain hysteresis observed for the 164- and 174-GHz channels, which are located in the same arm of the power divider chain. However, calibrated TAs computed showed that the radiometer external calibration allows us to calibrate out the transition and has no impact on the calibrated TA or on the NEDT. The instrument was flown as-is. Fig. 33 shows the radiometric counts jump observed in the 164- and 174-GHz channels and the calibrated TA resilient to any transitions in the raw counts. The blue and green curves show the counts during ramp down. The yellow and cyan curves show the counts during ramp up.

V. Conclusion

The TEMPEST-D mission has successfully demonstrated the first cross-track scanning millimeter-wave radiometer from 87 to 181 GHz based on 35-nm InP HEMT LNA technology in a direct-detection architecture. This is also the first millimeter-wave radiometer to utilize external, end-to-end calibration using two calibration sources in a 6U CubeSat. This low-mass, power, and volume implementation with the state of the art or better noise performance paves the way for a constellation of well-calibrated radiometers for temporal sampling of rapidly evolving storms. The external calibration measurements during each revolution of the scanning radiometer provide a very stable and well-calibrated radiometer on-orbit. The prelaunch calibration measurements of the TEMPEST-D radiometer provided an accurate characterization of the radiometric gain, bandpass, and receiver linearity. In addition, detailed measurements of the antenna patterns as well as scan bias and sidelobe contamination were performed.

The small size of the instrument provided the opportunity to perform many measurements with the integrated system that are not possible with larger instruments due to their inflexibility in test configuration. As an example, detailed measurements of the spectral response for each operating channel through the optics of the entire integrated radiometer by injecting and sweeping the frequency were made possible by this compact instrument implementation. The TEMPEST-D radiometer is a well-calibrated radiometer with the state of the art or better noise and radiometric sensitivities at these operating frequencies. It was developed for a fraction of the cost and length of schedule of traditional flagship mission instruments.

Acknowledgment

The authors would like to acknowledge Michelle Easter, Joelle Cooperrider, Mary Soria, Heather Lim, and Luca Lasagni, Jet Propulsion Laboratory (JPL), Pasadena, CA, USA, for their exceptional work contributing to the instrument development and the Temporal Experiment for Storms and Tropical Systems Technology Demonstration (TEMPEST-D) Team, Blue Canyon Technologies (BCT), who built and operated the TEMPEST-D satellite bus. They would like to thank Prof. Chris Ruf, Prof. V. Chandrasekar, Dr. Robert Jarnot, Dr. Wesley Berg, and Dr. Pekka Kangaslahti, for their advice and support. They would also like to acknowledge and thank Pamela Millar and Robert Bauer of NASA's Earth Science Technology Office (ESTO), Greenbelt, MD, USA, as well as George Komar, former Director of ESTO. All of the instrument development was performed at JPL, California Institute of Technology. ©2020. California Institute of Technology. Government sponsorship acknowledged.

References

[1] S. Padmanabhan *et al.*, "A 6U CubeSat constellation concept for atmospheric temperature and humidity sounding," in *Proc. United States Nat. Committee URSI Nat. Radio Sci. Meeting (USNC-URSI NRSM)*, Jan. 2014, p. 1.

[2] S. C. Reising *et al.*, "Overview of temporal experiment for storms and tropical systems (TEMPEST) CubeSat constellation mission," in *IEEE MTT-S Int. Microw. Symp. Dig.*, May 2015, pp. 1–4.

[3] P. Kangaslahti, D. Pukala, T. Gaier, W. Deal, X. Mei, and R. Lai, "Low noise amplifier for 180 GHz frequency band," in *IEEE MTT-S Int. Microw. Symp. Dig.*, Jun. 2008, pp. 451–454.

[4] S. T. Brown *et al.*, "The high-altitude MMIC sounding radiometer for the global hawk unmanned aerial vehicle: Instrument description and performance," *IEEE Trans. Geosci. Remote Sens.*, vol. 49, no. 9, pp. 3291–3301, Sep. 2011.

[5] D. J. Hoppe *et al.*, "A three-frequency feed for millimeter wave radiometry," *Microw. Opt. Technol. Lett.*, vol. 54, no. 11, pp. 2483–2487, Nov. 2012.

[6] R. E. Cofield and P. C. Stek, "Design and field-of-view calibration of 114-660-GHz optics of the Earth observing system microwave limb sounder," *IEEE Trans. Geosci. Remote Sens.*, vol. 44, no. 5, pp. 1166–1181, May 2006.

[7] M. Varonen *et al.*, "160-270-GHz InP HEMT MMIC low-noise amplifiers," in *Proc. IEEE Compound Semiconductor Integr. Circuit Symp. (CSICS)*, Oct. 2012, pp. 1–4.

[8] *HSCH-9161 GaAs Detector Diode*, Keysight Technol., Santa Rosa, CA, USA, Dec. 2017. [Online]. Available: https://www.keysight.com/us/en/assets/7018-01511/data-sheets/5989-6228.pdf.

[9] HRL Laboratories. *V1A Datasheet*. Accessed: Jun. 28, 2019. [Online]. Available: https://mmics.hrl.com/_assets/datasheet/V1A.pdf

[10] OMMIC. *CGY2870AUH/C1*. Accessed: Feb. 19, 2019. [Online]. Available: https://www.ommic.com/datasheets/OMMIC_DATASHEET_ZBD_CGY2870AUH-C1.pdf

[11] E. Kim, C.-H.-J. Lyu, K. Anderson, R. V. Leslie, and W. J. Blackwell, "S-NPP ATMS instrument prelaunch and on-orbit performance evaluation," *J. Geophys. Res. Atmos.*, vol. 119, no. 9, pp. 5653–5670, May 2014.

[12] W. Berg *et al.*, "Calibration and validation of the TEMPEST-D CubeSat radiometer," *IEEE Trans. Geosci. Remote Sens.*, early access, Sep. 9, 2020, doi: 10.1109/TGRS.2020.3018999.

[13] *General Environmental Verification Standard*. Accessed: Apr. 22 2013. [Online]. Available: https://standards.nasa.gov/standard/gsfc/gsfc-std-7000.

Sharmila Padmanabhan (Senior Member, IEEE) received the Ph.D. degree from Colorado State University, Fort Collins, CO, USA, in 2009.

She is a Section Staff Member with the Instrument Electronics and Software Section, Jet Propulsion Laboratory, California Institute of Technology, Pasadena, CA, USA. Her research interests include millimeter, submillimeter-wave, and infrared instrumentation for remote sensing, calibration/validation and performance assessment of microwave radiometers, and geophysical retrieval algorithm development.

Dr. Padmanabhan was a recipient of the NASA Exceptional Public Achievement Medal in 2019.

Todd C. Gaier received the Ph.D. degree in physics [studying the cosmic microwave background (CMB)] from the University of California at Santa Barbara, Santa Barbara, CA, USA, in 1993.

He is a Jet Propulsion Laboratory (JPL) Fellow, a Senior Research Scientist, and the Deputy Director for Astronomy and Physics at JPL, as well as a Faculty Associate in astronomy with the California Institute of Technology, Pasadena, CA. He has worked on technologies and instruments using monolithic microwave integrated circuit (MMIC) components operating at frequencies of 1–250 GHz. His projects include the Planck-LFI mission to study the anisotropy and polarization of the cosmic microwave background (CMB); the Q/U Imaging Experiment (QUIET) exploring the polarization of the CMB; Geostationary Synthetic Thinned Array Radiometer (GeoSTAR), an interferometric synthetic aperture imager for Earth atmospheric sounding from geostationary orbit; and the Advanced Microwave Radiometers for the Jason III mission mapping small variations in sea level across the globe monitoring conditions such as El Niño, the integrated receivers for the Juno Microwave Radiometers, the Compact Ocean Wind Vector Radiometer, a low-cost alternative to ocean wind measurement, and Temporal Experiment for Storms and Tropical Systems Technology Demonstration (TEMPEST-D), a CubeSat demonstrator for a mission to study temporal behavior of clouds and precipitation. His research interests include millimeter-wave electronics for applications in astrophysics and Earth remote sensing.

Alan B. Tanner is a Principal Engineer with the NASA's Jet Propulsion Laboratory, California Institute of Technology, Pasadena, CA, USA, where he has been employed since 1989. He specializes in the design and calibration of microwave radiometers and scatterometers for remote sensing of the Earth. He has been the Lead System Engineer for the Geostationary Synthetic Thinned Array Radiometer (GeoSTAR), the Ultra-Stable Radiometer testbed (which formed the basis of the Aquarius and Juno radiometer designs), the Advanced Water Vapor Radiometers (AWVRs) for the Cassini Gravitational Wave Experiment, the Airborne Cloud Radar (a 94-GHz scatterometer which preceded the CloudSat mission), and the Airborne Rain Mapping Radar (for Tropical Rainfall Measurement Mission). He held his graduate work at the Microwave Remote Sensing Laboratory (MIRSL), University of Massachusetts, Amherst, MA, USA, where he developed the Electronically Scanned Thinned Array Radiometer (ESTAR) for soil moisture measurements and the Stepped Frequency Microwave Radiometer (SFMR) for hurricane wind speed detection.

Shannon T. Brown (Senior Member, IEEE) received the B.S. degree in meteorology from Pennsylvania State University, State College, PA, USA, in 2001, and the M.S. degree in atmospheric science and the Ph.D. degree in geoscience and remote sensing from the University of Michigan, Ann Arbor, MI, USA, in 2003 and 2005, respectively.

He joined the Microwave Advanced Systems Section, Jet Propulsion Laboratory (JPL), Pasadena, CA, USA, in 2005, as a member. He is a Principal Technologist with NASA JPL. He has been involved in the spaceborne Topex; Jason-1, 2, and 3 Microwave Radiometers; and the WindSat Polarimetric Radiometer. He is a Principal Investigator of the Compact Ocean Wind Vector Radiometer being developed for the U.S. Air Force and an Instrument Scientist for the NASA Juno Microwave Radiometer on the Juno New Frontiers mission to Jupiter. He is a member of the Ocean Surface Topography Science Team, the Ocean Salinity Science Team, the SMAP Science Team, and the Juno Science Team. His research interests include microwave radiometer system development, calibration, geophysical algorithm development for both passive and active sensors, extraction of climate data records, and radiometer science.

Dr. Brown was a recipient of the NASA Exceptional Achievement Medal in 2009, the JPL Lew Allen Award in 2010, eight NASA group achievement awards, and the NASA Space Act Award in 2012.

Boon H. Lim (Senior Member, IEEE) received the B.S. and M.S. degrees in electrical engineering and the Ph.D. degree in geoscience and remote sensing from the University of Michigan (UMich), Ann Arbor, MI, USA, in 1999, 2001, and 2008, respectively.

He is the Project Systems Engineer and a NASA Engineering Technical Authority for PREFIRE with the Jet Propulsion Laboratory, California Institute of Technology (Caltech), Pasadena, CA, USA, where he has worked on and developed a variety of instruments, including GEOSTAR, HAMSR, MTHP, and RACE, and also occasionally lecturers on aerospace engineering. He is one of the lucky few to have successfully had his instruments ground-based, airborne, and spaceborne, and unluckily, lost at launch.

Steven C. Reising (Senior Member, IEEE) received the B.S.E.E. (*magna cum laude*) and M.S.E.E. degrees in electrical engineering from Washington University, St. Louis, MO, USA, in 1989 and 1991, respectively, and the Ph.D. degree in electrical engineering from Stanford University, Stanford, CA, USA, in 1998.

He served as an Assistant Professor of Electrical and Computer Engineering with the University of Massachusetts Amherst, Amherst, MA, USA, where he received tenure. He served as a Summer Faculty Fellow for three summers with the Remote Sensing Division, Naval Research Laboratory, Washington, DC, USA. He joined Colorado State University (CSU), Fort Collins, CO, USA, in 2004, where he served as an Associate Professor from August 2004 to June 2011, and has been a Full Professor of Electrical and Computer Engineering since July 2011. His research interests span a broad range of remote sensing disciplines, including microwave remote sensing of the Earth's atmosphere and oceans from airborne platforms, small satellites, and CubeSats; the design and development of radiometer systems from microwave to submillimeter-wave and THz frequencies (18–850 GHz); Lidar systems for sensing temperature and winds in the middle and upper atmosphere; and lightning-ionosphere interactions and atmospheric electrodynamics. He has been a Principal Investigator of 17 grants from NASA, NOAA, the National Science Foundation (NSF), the Office of Naval Research (ONR), National Polar-Orbiting Operational Environmental Satellite System Integrated Program Office (NPOESS), European Space Agency, and Ball Aerospace and FIRST RF.

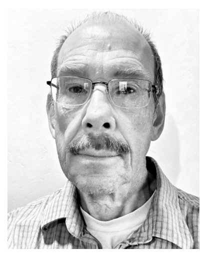

Robert Stachnik received the Ph.D. degree in physical chemistry from the University of California at Berkeley, Berkeley, CA, USA, in 1981.

He is a Research Scientist with the Laboratory Studies and Atmospheric Observations Group, Earth Science Division, Jet Propulsion Laboratory, California Institute of Technology, Pasadena, CA. His research interests include atmospheric composition and chemistry, development of remote-sensing millimeter-wave instrumentation, airborne and balloon field observations, and retrieval analysis.

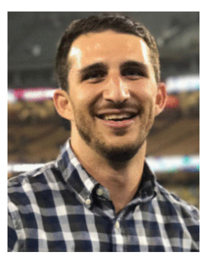

Rudi Bendig received the B.S. and M.S. degrees in electrical engineering from California Polytechnic State University, San Luis Obispo, CA, USA, in 2014.

He was with the Jet Propulsion Laboratory (JPL), Pasadena, CA, where he was involved in CubeSat programs to develop and test electronics, firmware, and software. He is an Electrical Engineer with NASA JPL. His research interests include the development of new and robust electronic technologies for the CubeSat and SmallSat form factor, these include field-programmable gate array (FPGA) and software implementations of novel algorithms to the remote sensing field. He has been on the development and test teams for RACE, MarCO, TEMPEST-D, and CubeRRT, as well as supported instruments for large projects including the Sentinel-6 motor electronics and the M2020 instrument MOXIE.

Mr. Bendig was a recipient of the NASA Group Achievement Award in 2016.

Richard Cofield (Life Member, IEEE) received the B.S. degree in applied physics from the California Institute of Technology, Pasadena, CA, USA, in 1974, and the M.S. degree in electrical engineering from the University of Southern California, Los Angeles, CA, in 1982.

In 1978, he joined the Jet Propulsion Laboratory, Pasadena, to design, analyze, and calibrate antenna and optical systems for spaceborne radar and radiometer instruments observing the Earth. His interests include reflector antennas and quasi-optical feed systems.